J Eng Math (2019) 114:65–86
https://doi.org/10.1007/s10665-018-9982-6

# Electromagnetic heating control via high-frequency resonance of a triple-layer laminate

**J. M. Gaone · B. S. Tilley · V. V. Yakovlev**

Received: 3 July 2018 / Accepted: 12 December 2018 / Published online: 4 January 2019


**Abstract** Beamed energy transport requires the use of heat exchangers to collect the thermal energy produced from the absorption of electromagnetic radiation. To explore the high-frequency effects of wave–geometry interactions on this heat transfer, we consider a central dielectric layer, possessing a temperature-dependent loss factor, surrounded by two fluid channels filled with a lossless dielectric fluid. Considering an asymptotically thin domain, we derive a diffusion–reaction equation, assuming no flow in the fluid. We show that the high-frequency effects generate a new energy balance leading to a previously unknown steady-state solution. A characterization of the steady-state-dependent parameters is performed in an effort to determine a mechanism to control the nonlinear heating. Diffusive effects are shown to produce regions of the power response where steady-state solutions are replaced by traveling-wave solutions. These regions are also location to the greatest heating efficiency. Analytical approximations to the wave speed and location of these regions are found using boundary layer theory.

**Keywords** Microwave heating · Photonic crystal · Thermal runaway

## 1 Introduction

Electromagnetic (EM) heating has been used for decades in thermal food applications [1], chemical processes [2], material processing [3–5] and a variety of industrial heating applications [6]. EM heat exchangers absorb EM radiation and transfer heat to a fluid which can be collected to do work. These devices have been studied in context of solar energy collection [7], but lack the rigorous analysis needed to understand the underlying physics. In recent years, EM heat exchangers have been considered as a possible way to harness beamed energy [8]. Many properties can affect the operation of heat exchangers such as geometry, thermal and electrical properties, as well as the complexities involved in the coupling of EM, thermal, and fluid transfer equations.

J. M. Gaone · B. S. Tilley (✉) · V. V. Yakovlev
Center for Industrial Mathematics and Statistics, Department of Mathematical Sciences, Worcester Polytechnic Institute, 100 Institute Rd., Worcester, MA 01609, USA
e-mail: tilley@wpi.edu

J. M. Gaone
e-mail: jmgaone@wpi.edu

V. V. Yakovlev
e-mail: vadim@wpi.edu

The motivation for this work is a heat exchanger which converts EM energy into thermal energy, which is transferred to a coolant and whose energy is then used for mechanical work. Such an application has numerous physical mechanisms which take place simultaneously, and a full understanding of these interactions needs a foundation on which additional results can be related. This work is such an approach, and with that we consider an idealized heat exchanger, shown in Fig. 1, where an electromagnetically lossy material is surrounded by two lossless materials (e.g., coolant). Our focus in this work is on how the geometry of the widths of the materials affects the EM heating of this system, and we neglect the temperature dependence of the material properties in the coolant (regions 2 and 4 shown in Fig. 1).

Mathematical models of EM heating have been extensively studied in the past 40 years, but in cases when the wavelength is much longer than the problem geometry without considering high-frequency interactions [9,10]. Unique phenomena occur when the wavelength is comparable to the microscale structure of a material, which is seen in the field of photonics. Despite this, photonics studies generally have not considered heating, but rather mainly focus on optical effects. We examine the effect EM heating has on a material when exhibiting high-frequency phenomena.

Microwave heating was discovered after WWII and became an area of intense research after the invention of the microwave oven discovery of microwave heating by Percy Spenser in 1945 [11]. At high temperatures, a limit of the technology has been the phenomenon of thermal runaway. Thermal runaway is an inherent EM heating effect characterized by rapid uncontrollable heating [12–18]. It can lead to the destruction of the target material, either through fracturing from thermal stress or deformation by melting. Thermal runaway is caused by the fact that the rate the EM energy is absorbed by the dielectric material increases at higher temperatures which in turn increases temperature further creating a positive feedback. There have been many attempts to control thermal runaway [13,14,16,18–21] that is necessary to attain efficient heating while avoiding damaging effects.

Mathematical modeling of microwave heating did not start until the early 1990s. One of the first main results was a model by Kriegsmann et al., which resulted in a bifurcation diagram known as the S-curve power response curve (or also known as the S-curve) which could explain thermal runaway in a mathematical context.

The S-curve was originally found for a half-space dielectric medium [22], then again for an infinite slab [9], and later for an infinite three-layer laminate [10]. These models assume the wavelength is much longer than the width of the layers as well as consider the asymptotic limit where the three layers are sufficiently thin that the temperature in $z$ across the width of the system remains constant. In this paper, we describe the three-layer model and explain the dominant balance of the resulting S-curve. We extend this analysis to consider widths which are comparable to the wavelength of the applied radiation.

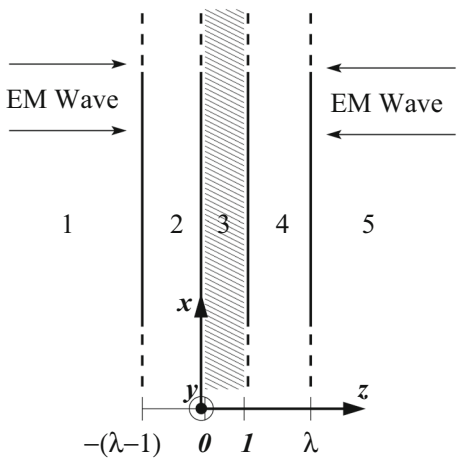


**Fig. 1** Triple-layer laminate infinite strip domain. Regions 1 and 5 are free-space, regions 2 and 4 are a lossless dielectric, and region 3 is a lossy dielectric. Unit cell defined as two layers from [0, λ]. Symmetric, monochromatic, polarized plane waves impinge the external boundaries at normal incidence

We begin by reviewing past work considering the microwave heating of a triple-layer laminate on an infinite strip domain where a single absorbing dielectric layer is surrounded by two lossless dielectric layers. In this work, we introduce a fundamental model of a heat exchanger by considering the two lossless layers are fluid channels, which for the extent of this work will not exhibit any fluid flow. Two models are developed to study different aspects of heating the triple-layer laminate. Section 2 introduces a triple-layer model considering high-frequency illumination where the EM field wavelength is comparable to the width of the layers. We employ the same asymptotic approach as done by Kriegsmann et al. [22], assuming thin layers to produce a uniform temperature in one dimension, while the temperature profile is examined under uniform heating in the other dimension. Section 3 considers a finite domain exhibiting nonuniform heating by applying a Dirichlet condition at one end of the laminate. The next model discussed in Sect. 4 considers a direct numerical solution of the governing equation using the Peaceman–Rachford-alternating direction implicit (PR-ADI) method which makes no assumption on the scale of parameters and considers spatial temperature variations in $z$ across the width of the system. The two mathematical models are then compared with each other where differences in the power responses have been explained by [23]. Concluding remarks summarizing the main results and validation are presented in Sect. 5.

## 2 Thin domain asymptotics: uniform heating

Consider the three-layer laminate depicted in Fig. 1 with plane waves symmetrically impinging the material from both sides at normal incidence. The EM waves, governed by Maxwell's equations, propagate through the lossy material which generates heat. Maxwell's equations are reduced to solving the 1D Helmholtz equation:

$$\frac{\partial^2 E_j}{\partial z^2} + \gamma^2 \epsilon E_j = 0, \tag{1}$$

where $E_j$ is the electric field strength of a field polarized in $y$, within region $j = 1, 2, 3, 4, 5$, and subject to boundary conditions:

$$\lim_{z\to-\infty}\left(\frac{\partial}{\partial z} + \mathrm{i}\gamma\right)(E_1 - E_{\text{inc}}) = 0, \tag{2}$$

$$E_1 = E_2, \quad \frac{\partial E_1}{\partial z} = \frac{\partial E_2}{\partial z}, \quad z = -(\lambda - 1), \tag{3}$$

$$E_2 = E_3, \quad \frac{\partial E_2}{\partial z} = \frac{\partial E_3}{\partial z}, \quad z = 0, \tag{4}$$

$$E_3 = E_4, \quad \frac{\partial E_3}{\partial z} = \frac{\partial E_4}{\partial z} \quad z = 1, \tag{5}$$

$$E_4 = E_5, \quad \frac{\partial E_4}{\partial z} = \frac{\partial E_5}{\partial z}, \quad z = \lambda, \tag{6}$$

$$\lim_{z\to\infty}\left(\frac{\partial}{\partial z} - \mathrm{i}\gamma\right)(E_5 - E_{\text{inc}}) = 0, \tag{7}$$

where $\gamma = \frac{2\pi l}{\lambda_0}$ is a nondimensional wavenumber, $l$ is the width of region 3, $\lambda_0$ is the free space wavelength, $E_{\text{inc}}$ is the incident electric field, and $\epsilon = \epsilon' + \mathrm{i}\epsilon''(T)$ is the complex dielectric constant. The long-wave regime, where $\gamma \ll 1$, was studied by [22] whereas the high-frequency regime, where $\gamma = O(1)$, is considered in this work. Equations (2) and (7) are Sommerfeld's radiation conditions, while Eqs. (3)–(6) are continuity and continuity of the derivative of the electric field, which are derived from the classical boundary conditions of the electric and magnetic fields across a material interface [24,25]. The electric field can be solved for exactly and takes the form

$$E_j(z) = a_j \mathrm{e}^{\mathrm{i}\gamma\sqrt{\epsilon_j}z} + b_j \mathrm{e}^{-\mathrm{i}\gamma\sqrt{\epsilon_j}z}. \tag{8}$$

While we acknowledge that the temperature dependence of the real permittivity $\epsilon'$ and the dielectric loss $\epsilon''$ are known to vary with temperature changes, we only consider the dependence on the loss factor for these models. We

have chosen to hold the permittivity constant in this model in order to investigate how the temperature dependence of the dielectric loss affects the power response of this system. Future work that aims to consider the temperature dependence of the permittivity is relevant, and we quantify the potential effects of this dependence in our parametric study of the current model in Sect. 2.2.

We are interested in cases when the heat losses from the laminate system to the environment are minimal. This suggests that the time scale for conduction in the $z$-direction is much shorter than that for thermal conduction in the $x$-direction. To implement this assumption in the analysis below, we scale time on $L^2/\alpha_3$, since we are interested in cases where thermal conduction across the layer width ($z$-axis) is instantaneous compared to the conduction in the $x$-direction.

We nondimensionalize $T$ by the transformation $T \to (T - T_\mathrm{A})/T_\mathrm{A}$ so that the nondimensional $T$ below represents the scaled temperature deviation from the ambient temperature $T_\mathrm{A}$. We scale $x$ on $L$, the characteristic length, and $z$ on $l$, the characteristic width, and $t$ on $\frac{L^2}{\alpha_3}$, the characteristic time of diffusion along the length, where $\alpha_3$ is the thermal diffusivity of region 3. The nondimensional energy equations in each of the layers are given by

$$\frac{\partial T_2}{\partial t} = \alpha\left(\frac{\partial^2 T_2}{\partial x^2} + \frac{1}{\eta^2}\frac{\partial^2 T_2}{\partial z^2}\right), \quad (x, z) \in (-\infty, \infty) \times [-(\lambda - 1), 0], \tag{9}$$

$$\frac{\partial T_3}{\partial t} = \frac{\partial^2 T_3}{\partial x^2} + \frac{1}{\eta^2}\frac{\partial^2 T_3}{\partial z^2} + P\sigma_3(T_3)|E_3|^2(T_3), \quad (x, z) \in (-\infty, \infty) \times [0, 1], \tag{10}$$

$$\frac{\partial T_4}{\partial t} = \alpha\left(\frac{\partial^2 T_4}{\partial x^2} + \frac{1}{\eta^2}\frac{\partial^2 T_4}{\partial z^2}\right), \quad (x, z) \in (-\infty, \infty) \times [1, \lambda], \tag{11}$$

with boundary conditions

$$K\frac{\partial T_2}{\partial z} = \eta^2 Bi\, T_2 + \eta^2 R[(T_2 + 1)^4 - 1], \quad z = -(\lambda - 1), \tag{12}$$

$$T_2 = T_3, \quad K\frac{\partial T_2}{\partial z} = \frac{\partial T_3}{\partial z}, \qquad z = 0, \tag{13}$$

$$T_3 = T_4, \quad \frac{\partial T_3}{\partial z} = K\frac{\partial T_4}{\partial z}, \qquad z = 1, \tag{14}$$

$$-K\frac{\partial T_4}{\partial z} = \eta^2 Bi\, T_4 + \eta^2 R[(T_4 + 1)^4 - 1], \; z = \lambda, \tag{15}$$

$$T_{2,3,4} \text{ bounded}, \tag{16}$$

$$T_{2,3,4}(0, x, z) = 0, \tag{17}$$

where $T_j$ is the temperature in region $j$, $\eta = \ell/L$ is the aspect ratio of the system, $\alpha = \frac{\alpha_2}{\alpha_3}$ is the ratio of thermal diffusivities, $P = L^2 E_0^2 \epsilon_0 \omega/(2T_\mathrm{A} k_3)$ is a nondimensional power of the incident electric field, $K = \frac{k_2}{k_3} = \frac{k_4}{k_3}$ is the ratio of thermal conductivities, $\eta^2 Bi = \frac{hl}{k_3}$ is a Biot number (energy loss from external convection), and $\eta^2 R = s\varepsilon l T_\mathrm{A}^3/k_3$ is a radiation parameter (energy loss from blackbody radiation) . The external losses are assumed to be small and scaled by $\eta^2$, so that $Bi$, $R = O(1)$, which is to say heat transfer from the laminate system is negligible at leading order and the first correction. Equations (12) and (15) represent energy lost to the external environment via Newton's law of cooling and the Stefan–Boltzmann law, Eqs. (13) and (14) are continuity and continuity of thermal flux, Eq. (16) ensures temperature is bounded as $|x| \to \infty$, and Eq. (17) sets the initial temperature to the ambient temperature. The dimensional parameters include thermal diffusivity $\alpha_j = k_j/(\rho_j c_{\mathrm{p}_j})$, thermal conductivity $k_j$, density $\rho_j$, heat capacity $c_{\mathrm{p}_j}$, characteristic incident electric field intensity $E_0$, permittivity of free space $\epsilon_0$, angular frequency $\omega$, ambient temperature $T_\mathrm{A}$, heat transfer coefficient $h$, Boltzmann constant $s$, and emissivity $\varepsilon$.

Equations (9)–(11) show that the Laplacian in $z$ is scaled by $\eta^{-2}$. Under the asymptotic assumption of a thin laminate $\eta \ll 1$, the temperature is expanded in the asymptotic series $T = T^{(0)} + \eta T^{(1)} + \eta^2 T^{(2)} \cdots$ where the system is solved sequentially.

The six leading-order and first-order correction problems are given by

$$\frac{\partial^2 T_j^{(0)}}{\partial z^2} = 0, \quad \frac{\partial^2 T_j^{(1)}}{\partial z^2} = 0, \tag{18}$$

representing the leading-order and first-order correction solutions, and $j = 2, 3, 4$, representing the three material layers. The solutions of each are linear in $z$. Applying the boundary conditions (12)–(15) shows that the leading order $T^{(0)}(t, x)$ and first correction $T^{(1)}(t, x)$ solutions are independent of $z$. At the next order, compatibility yields an averaged equation for the leading order solution $T^{(0)}$ by integrating each equation over the $z$ domain and applying boundary conditions (see Appendix A). The leading order problem is then given by

$$\overline{\rho c_p}\frac{\partial T}{\partial t} = \overline{k}\frac{\partial^2 T}{\partial x^2} + P\sigma_3(T)\|E_3\|_2^2(T) - 2\mathcal{L}(T), \tag{19}$$

where $\overline{\rho c_p} = 1 + 2(\lambda - 1)\frac{K}{\alpha}$ is the effective heat capacity per unit volume, $\overline{k} = 1 + 2(\lambda - 1)K$ is an effective thermal conductivity, and $\mathcal{L}(T) = Bi\, T + R[(T + 1)^4 - 1]$ is the external energy loss due to external convection and blackbody radiation, respectively. The squared norm of the electric field is defined as $\|E_3\|_2^2 = \int |E_3|^2 \, \mathrm{d}z$ and $|E_3|^2 = E_3\, E_3^*$, where $E_3^*$ is the complex conjugate of $E_3$. The result of the thin domain assumption is that the evolution of temperature will depend only on time and in $x$. Furthermore, we assume that the electric field is uniformly applied along $x \in (-\infty, \infty)$. This implies the diffusive thermal flux, $\overline{k}\frac{\partial T}{\partial x}$, is zero so the resulting equation governing the average temperature is

$$\overline{\rho c_p}\frac{\partial T}{\partial t} = P\sigma_3(T)\|E_3\|_2^2(T) - 2\mathcal{L}(T), \tag{20}$$

which can also be obtained using zero flux Neumann conditions in $x$ on the finite domain described in Sect. 3. We now define the power response curve as the steady-state bifurcation diagram of $(P, T)$, where $T$ is the steady-state temperature satisfying

$$P = \frac{2\mathcal{L}(T)}{\sigma_3(T)\|E_3\|_2^2(T)}. \tag{21}$$

Many dielectric materials have been empirically found to posses effective electric conductivities that exponentially increase in temperature, $\sigma_3 = A_3 \mathrm{e}^{b_3 T}$. Appendix B shows a least squares curve fit for this functional form to data of two samples taken from [18,26]. It is under this assumption that Kriegsmann et al. [22] found the power response curve defined as (21) to be S-shaped as shown in Fig. 3a. It was later proven by Pelesko and Kriegsmann that the positively sloped branches of the power response curve are stable while the negatively sloped branch is unstable [10]. As power is increased past the lower branch, thermal runaway takes over and heats the material to the temperature at the upper branch. The only two stable states are for low temperatures, which is inefficient heating, and high temperatures, which may damage the material.

One attempt at controlling this thermal runaway event was to build in a feedback control that increases the device to high powers increasing the temperature and then quickly decrease to low powers to bring the temperature back down [9]. The cyclic heating and cooling would oscillate around medium temperatures. This method is difficult to implement in practice.

The S-curve model described was for wavelengths much longer than width of the layers. In our previous work [19] examined more thoroughly here, we consider the case where the wavelength is comparable to the width of the layers. We choose the wavelength, permittivity, and layer width to satisfy the following: outer layer width is an odd multiple of a quarter wavelength $l(\lambda - 1) = (2m - 1)\frac{\lambda_2}{4}$ and the inner layer width is an odd multiple of a half wavelength $l = (2n - 1)\frac{\lambda_3}{2}$, where $\lambda$ is the nondimensional width of a unit cell, $n, m \in \mathbb{Z}^+$, and $\lambda_j$ is the wavelength in region $j$. The unit cell is defined by the domain $[0, \lambda]$. A commonly used term in homogenization

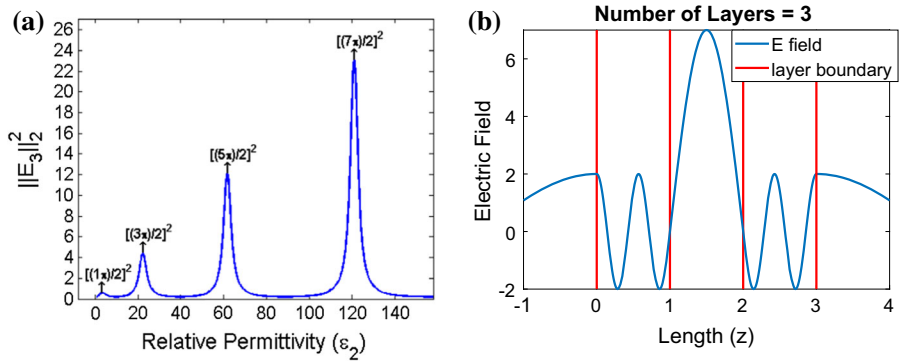


**Fig. 2** Electric field strength in middle lossy layer (region 3) as a function of the outer layer permittivity. Peaks show Bragg resonance states with increasing field strength (**a**). Electric field (blue) within the triple-layer laminate boundaries (red) at resonance state. Middle layer shows large electric field from applied resonance (**b**). (Color figure online)

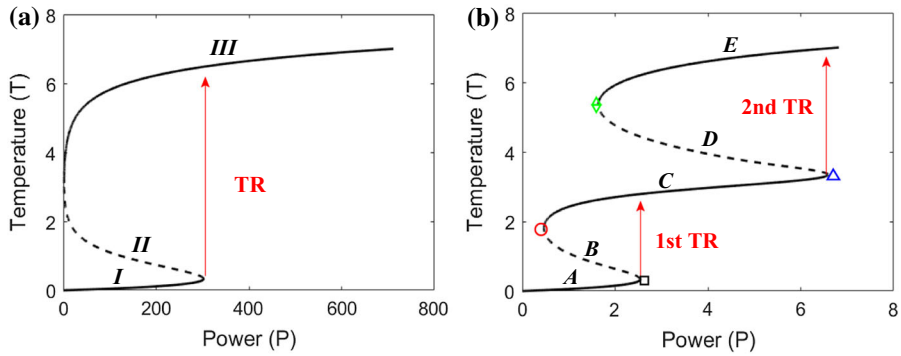


**Fig. 3** Power response depicting S-curve where no resonance occurs for $\epsilon_2 = 9\pi^2$ (**a**). The three branches are labeled with uppercase roman numerals $I$, $II$, $and III$. The red arrow labeled 'TR' indicates the thermal runaway event. Power response depicting Double-S-curve, where resonance is established for $\epsilon_2 = \left(\frac{7\pi}{2}\right)^2$ (**b**). The five branches are labeled with uppercase letters $A$, $B$, $C$, $D$, and $E$, and the four turning points are labeled first through fourth with colored symbols □, ○, △, and ◇ respectively. The two red arrows labeled 'TR' indicate the two separate thermal runaway events. Additional parameters for both graphs include $\epsilon_m = \pi^2$, $K = 0.5$, $Bi = 0.5$, $Q = 0$, $\sigma_3(T) = 10^{-3}e^{3T}$. (Color figure online)

theory, it is composed of the lossy layer and one of the lossless layers. These conditions are comparable to those for Bragg interference and Fabry–Pérot cavity, which establish a resonance and build up the electric field inside the middle layer, as shown by Fig. 2b. In addition, it is a well-known fact that this resonance is strengthened when there is high contrast between $\epsilon_2$ and $\epsilon_3$. Figure 2a shows the electric field strength as $\epsilon_3$ increases, thus increasing this contrast since $\epsilon_2 = \pi^2$. Resonance states show peaks in the electric field which increases as the contrast increases. This dramatic change in the electric field transforms the S-shaped power response curve to a Double-S-shaped power response introducing two additional steady-state branches one of which is stable. Figure 3a depicts an S-curve, while Fig. 3b shows a Double-S-curve, where the stable branches are plotted as solid lines and the unstable branches as dashed lines. The new stable branch occurs at the desired medium-range temperatures for efficient heating while avoiding the damaging effects of thermal runaway. In addition, the power scale is reduced by two orders of magnitude. This phenomenon provides the opportunity to control thermal runaway to our advantage. By increasing a low power just past the first right turning point, thermal runaway is induced, but comes to rest at a safe and efficient operating temperature on the middle branch.

A periodic geometry of high- and low-permittivity materials, which produce a band-gap structure and are now called photonic crystals, date back to studies by Rayleigh [27]. A defect in the crystal introduces a phase slip generating the resonance discussed above where such structures are known as a distributed Bragg reflector or a dielectric mirror with a defect. Construction of such photonic resonance cavities have been achieved at drastically

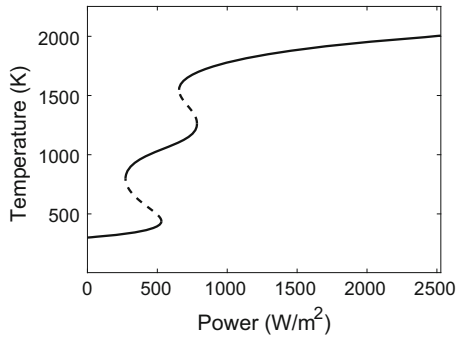


**Fig. 4** Power response curve of a triple layer laminate characterized by a layer of zirconia surrounded by two channels of glycerine

different scales, from microwave wavelengths [28,29] to optical wavelengths [30,31], allowing for a wide range of potential applications. To demonstrate this, we consider a dimensional scenario with a zirconia lossy middle layer of width 2.36 cm, which is adjacent to two 1.09 cm channels of fluid glycerine. The associated response curve plotting microwave input power flux in watts per square meter (W/m$^2$) against the temperature, measured in Kelvin (K), is provided in Fig. 4. The relative dielectric constant of zirconia is taken to be $\epsilon = 6.69 + \mathrm{i}0.0029128 \cdot 10^{2.3259\,T}$ [26] where the functional form of the loss factor is a least squares curve fit. The thermal conductivity of zirconia is $k_{\mathrm{zir}} = 0.3$ W/m K. The relative dielectric constant of a 100% glycerine solution is $\epsilon = 15 + \mathrm{i}0$ [32]. The thermal conductivity of glycerine is $k_{\mathrm{gly}} = 0.6$ W/m K and the heat-transfer coefficient is chosen to be $h = 0.5$ W/m$^2$ K [33]. Finally, the incident frequency is 22.6 GHz.

The temperature dependence of the real part of the dielectric constant is excluded in our analysis in order to examine the temperature effects of the imaginary part alone. A major consequence of applying this assumption to the results presented is that the resonance state also remains unchanged. Since the resonance conditions depend on the permittivity by considering it to be temperature dependent the resonance may degrade or even be broken. This poses an engineering challenge to implementing the steady-state mechanism described above. Materials whose permittivity is weakly temperature dependent would be favorable. Another possible solution might involve clever feats of engineering where multiple layers or cavities work together to cause multiple resonance states that occur at different temperatures. In this approach when one resonance state decays from temperature changes another would be generated in its place. Future work will be required in this area.

### 2.1 Stability mechanisms

How does the applied resonance of the electric field create the Double-S-curve? To answer this question, we first provide an explanation of the energy balance for the stability of each branch. We know steady states are given by the balancing of the sources to losses in Eq. (21). The turning points are where branches change and we can determine where they occur by the slope of $P(T)$, however, it is more convenient to consider it in the logarithmic scale. Thus the slope is determined by

$$\frac{\mathrm{d}[\ln(P)]}{\mathrm{d}T} = \underbrace{-\frac{1}{\|E_3\|_2^2}\frac{\partial\|E_3\|_2^2}{\partial T}}_{\text{(i)}} \underbrace{-\,b_3}_{\text{(ii)}} + \underbrace{\frac{1}{\mathcal{L}}\frac{\mathrm{d}\mathcal{L}}{\mathrm{d}T}}_{\text{(iii)}}, \tag{22}$$

where $b_3$ is the exponent in the effective conductivity $\sigma_3(T)$. Turning points occur when $\frac{\mathrm{d}[\ln(P)]}{\mathrm{d}T} = 0$, and stable (unstable) branches occur when $\frac{\mathrm{d}[\ln(P)]}{\mathrm{d}T} > (<)\,0$. Since the branch is determined by the balancing of these three terms we label each term, left to right, as (i), (ii), and (iii), respectively.

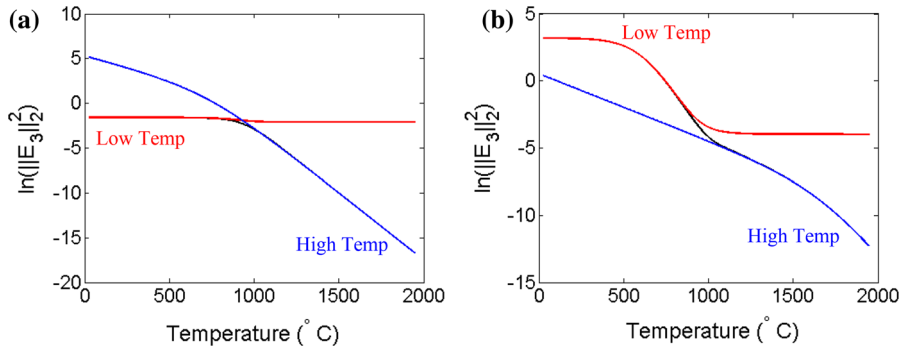


**Fig. 5** Natural logarithm of the electric field strength as a function of temperature without resonance (**a**) and with resonance (**b**) (black). Analytic approximations that are asymptotic at low temperatures (red) and at high temperatures (blue). (Color figure online)

Prior to discussing each branch in detail a few notes should be made. Firstly, the temperature dependence on $\|E_3\|_2^2$ is seen by Fig. 5. Secondly, since $\frac{\partial \|E\|_2^2}{\partial T} < 0$, (i) is always positive. Next, since $b_3$ is a constant, (ii) is constant, and finally since $\mathcal{L}(T)$ is a polynomial (iii) decreases with temperature like $T^{-1}$.

*Branch I* at these low temperatures the electric field does not attenuate much, so $\|E_3\|_2^2$ is large and its derivative is small making (i) negligible. Since the slope is positive (iii) $>$ $-$(ii), so branch I is *externally stabilized*. The external losses are able to match the rate at which energy is generated internally.

*Branch II* (i) remains small, but now, since (iii) decreases with temperature, the external losses can no longer remove energy at the same rate at which heat is generated making (iii) $<$ $-$(ii) yielding a negative slope and an unstable branch.

*Branch III* (iii) is negligible at high temperatures. The electric field having lost most of its energy to the material, $\|E_3\|_2^2$ is small while its derivative is also small since there is not much energy left to lose. This makes (i) comparable with (ii), but since it is stable we have that (i) $>$ $-$(ii). Branch III is called *conductively stabilized* [22], since the balance comes not from balancing heat generation to heat loss, but rather balancing increased absorption rate (from exponential conductivity) to less energy available (attenuated electric field).

These were the three branches found by Kriegsmann et al. [22] on the S-curve, and they are also seen on the Double-S-curve as well, where the same dominant balances producing branches I, II, and III of Fig. 3a are also responsible for branches A, B, and E of Fig. 3b. In order to understand the two new branches associated with the Double-S-curve, we first have to analyze how the electric field changes under resonance. The imaginary part of the wavenumber $k_3 = \sqrt{\epsilon_3}$ is given by

$$\mathrm{Im}(k_3) = \sqrt[4]{\epsilon_3'^{\,2} + A_3^2 \mathrm{e}^{2b_3 T}} \sin\left[\frac{1}{2}\arctan\left(-\frac{A_3 \mathrm{e}^{b_3 T}}{\epsilon_3'}\right)\right]. \tag{23}$$

We make two asymptotic approximations for low temperatures and high temperatures. When $T$ is small, $\mathrm{e}^{b_3 T} \approx 1$, and when $T$ is large $\arctan(-A_3 \mathrm{e}^{b_3 T}(\epsilon_3')^{-1}) \approx -\frac{\pi}{2}$, so we define approximate wavenumbers when temperature is small and when it is large as

$$\mathrm{Im}(k_3)_{T\ll 1} = \sqrt[4]{\epsilon_3'^{\,2} + A_3^2} \sin\left[\frac{1}{2}\arctan\left(-\frac{A_3 \mathrm{e}^{b_3 T}}{\epsilon_3'}\right)\right], \tag{24}$$

$$\mathrm{Im}(k_3)_{T\gg 1} = -\frac{\sqrt{2}}{2}\sqrt{A_3}\mathrm{e}^{\frac{b_3}{2}T}. \tag{25}$$

Figure 5 graphs the logarithm of the electric field strength as a function of temperature using Eq. (23), given by the black curve, Eq. (24), given by the red curve, and Eq. (25) given by the blue curve. Figure 5a shows the electric field without resonance, while Fig. 5b is with resonance. Immediately we notice two distinct differences between the two graphs. First, at resonance, we see a rapid decrease in the electric field at medium temperatures. Recall resonance is able to build up the electric field in the middle layer, essentially trapping energy within its boundary. It is this

build-up of the electric field that allows for this rapid loss of electric energy. Second, we notice that the slope of the field strength as a function of temperature is shallower for lower temperatures and then becomes more steep as the temperature increases. Compare this to the case without resonance, and the slope at high temperature remains steep throughout. Since we were able to solve the electric field exactly for this problem, the expression governing the high temperature behavior is

$$\|E_3\|_2^2 \propto \left[k_2^2 M^2 \mathrm{e}^{\frac{b_3}{2}T} + k_2 M \mathrm{e}^{b_3 T} + \mathrm{e}^{\frac{3}{2}b_3 T}\right]^{-1}, \tag{26}$$

where $k_2$ is the wave number in the lossy layer and $M$ is a compound reflection–transmission coefficient. For the case of no resonance $k_2 M \approx 1$, so the largest exponential $\mathrm{e}^{\frac{3b_3}{2}T}$ is dominant. During resonance, however, $k_2 M \gg 1$, so the lower-powered exponential, $\mathrm{e}^{\frac{b_3}{2}T}$, affects the solution in the middle temperature region, but eventually succumbs to the dominating effects of the exponential, $\mathrm{e}^{\frac{3b_3}{2}T}$, at the highest temperatures. We can now describe the two new branches.

*Branch C* The temperatures are not yet large enough to completely attenuate the electric field, so $\|E_3\|_2^2$ is still large, however, as we have shown in Fig. 5b its derivative has a large negative value. So large in fact that it forces (i) $>$ −(ii) making branch C stable. We say branch C is *rapid-attenuation stabilized* since the new mechanism stabilizing the branch is the rapid loss of EM energy within this temperature range.

*Branch D* The rapid loss of EM energy that stabilized branch C does have a narrow temperature range, making the derivative of $\|E_3\|_2^2$ smaller in magnitude once again at temperatures directly above this range. Equation (26) shows that in this region $\|E_3\|_2^2 \approx (k_2 M)^{-2}\mathrm{e}^{-\frac{b_3}{2}T}$, which causes (i) $= \frac{b_3}{2}$ so (i) $<$ −(ii) making branch D unstable. Once the temperature increases further so that $\|E_3\|_2^2 \approx \mathrm{e}^{-\frac{3b_3}{2}T}$, it makes (i) $= \frac{3b_3}{2}$ and corresponds to branch E.

## 2.2 Parametric study

Precise control of branch C is required in order for it to be a practical method of controlling the thermal runaway of EM heating. Next, we characterize the Double-S-curve through parametric studies of all the parameters on which the power response depends. The parameters can be categorized into two sets. The first set of parameters belongs to resonance parameters, those responsible for establishing resonance between the layers, which include, the permittivities $\epsilon_2'$ and $\epsilon_3'$, the unit cell width $\lambda$, and wavenumber $\gamma$. The second set belongs to the thermal parameters, which are responsible for the rate at which thermal energy is lost from or generated by the system. These parameters include the Biot number, $Bi$, the radiation parameter, $R$, the loss factor $A_3$, and the loss factor exponential $b_3$. Up to this point, we have considered the outer layers of regions 2 and 4 to be lossless, not absorbing any EM energy. We briefly consider the case when these layers are lossy having an effective conductivity: $\sigma_2 = \sigma_4 = A_2 \mathrm{e}^{b_2 T}$. The power response including the losses from the two additional layers is

$$P = \frac{2BiT + 2R[(T+1)^4 - 1]}{\sigma_2(T)\|E_2\|_2^2 + \sigma_3(T)\|E_3\|_2^2 + \sigma_4(T)\|E_4\|_2^2}. \tag{27}$$

This yields two additional parameters to characterize, the loss factor $A_2$, and loss factor exponential $b_2$. It is noteworthy that while most of the parameters must remain fixed, both $\gamma$ and $Bi$ can be varied during operation of beamed energy applications, providing possible mechanisms in controlling the EM heating process.

The first set of parameters controlling resonance are studied by plotting parametric curves of the temperature and power for the turning points of the power response. The plots are colored by line or by marker to match the color and symbol of the first □, second ○, third △, and fourth ◇ turning points labeled in Fig. 3b.

We begin by performing a parametric study of the permittivity of the lossless layers $\epsilon_2'$. Figure 6a graphs the temperature at the turning points while Fig. 6b graphs the power at the turning points against $\epsilon_2'$. It shows how the power response curve transforms from an S-curve to a Double-S-curve as $\epsilon_2'$ is far from or close to satisfying the resonant condition, as seen by the existence of two or four curves. The transformation occurs as the two top turning

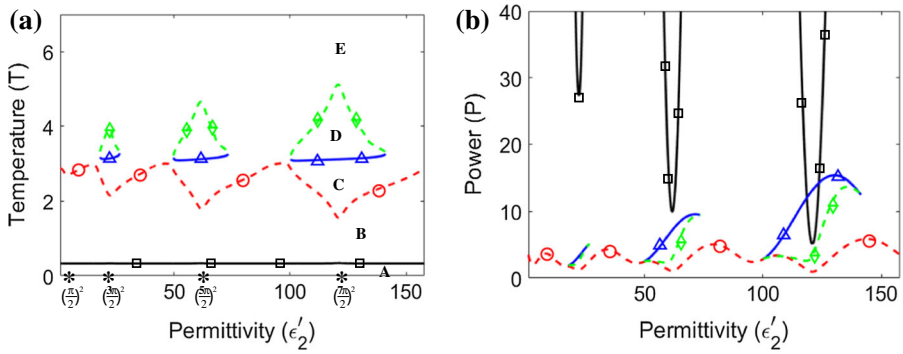


**Fig. 6** Parametric curves for temperature (**a**) and power (**b**) of the turning points of the power response curve as functions of the outer layer permittivity $\epsilon_2'$. Resonance states are labeled by an asterisk. Branches of Double-S-curve are labeled A–E

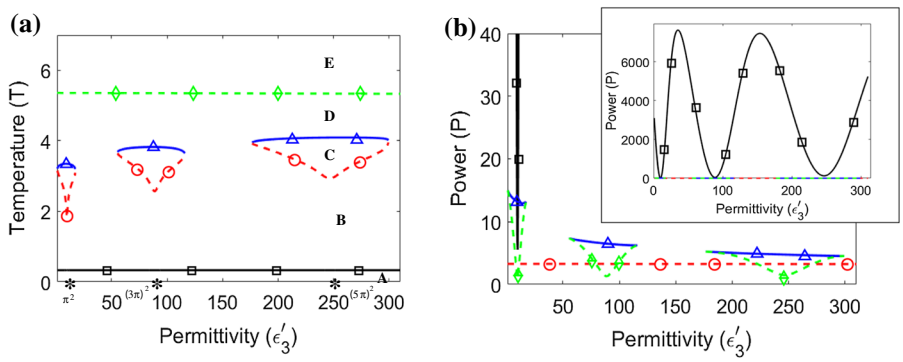


**Fig. 7** Parametric curves for temperature (**a**) and power (**b**) of the turning points of the power response curve as functions of the outer layer permittivity $\epsilon_3'$. Resonance states are labeled by an asterisk. Branches of Double-S-curve are labeled A–E. The inset shows how the power level of the first turning oscillates over a large range, with minima located at the resonance states

points are created and annihilated together in pairs. A significant result from Fig. 6b is that the first turning point occurs at very low powers when at resonance. This is a benefit as the low power would indicate an efficient method of initiating the first thermal runaway event to reach the middle branch of the Double-S-curve.

Similar parametric curves are plotted for the permittivity of the lossy layer $\epsilon_3'$ in Fig. 7. Once again we see the transformation from an S-curve to a Double-S-curve by the existence of two or four curves. However, Fig. 7a shows that by changing this particular parameter, the transformation occurs by the creation and annihilation of the middle two turning points in a pair.

Varying $\lambda$ changes the width of the lossless layer, or rather the ratio of the width of the lossless layer to the lossy layer since the domain has been nondimensionalized. Figure 8 shows the temperature of the turning points as a function of $\lambda$. The behavior of the turning points mirrors that of the outer permittivity in Fig. 6a. The only difference is that unlike the outer permittivity the strength of the resonance does not increase with every successive resonance state, instead it appears periodic.

The nondimensional wavenumber $\gamma$ includes the ratio of the width of the layer in region 3 to the free space wavelength. When the temperature of the turning points are plotted against $\gamma$ in Fig. 9, we witness a much different behavior. The first turning point persists alone for all values of $\gamma$, whereas the other three turning points will alternate the creation and annihilation of a pair of turning points as $\gamma$ approaches or recedes from resonance values. Label **a** shows the creation of the second and third turning points together where the third turning point is then annihilated with the fourth turning point at **b**. In contrast **c** shows the creation of the third and fourth turning point together where **d** shows the annihilation of the third and second turning points. Additionally, we see instances where turning points which used to be labeled as the second turning point at one resonance state become the fourth turning point

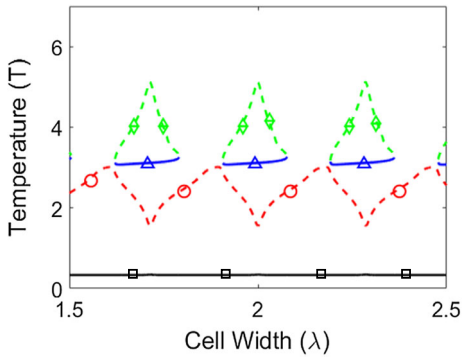


**Fig. 8** Parametric curve of temperature as a function of the unit cell width λ

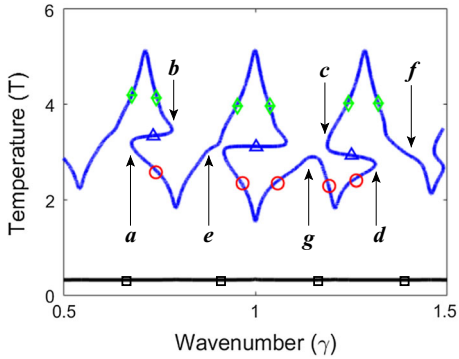


**Fig. 9** Parametric curve of temperature as a function of the wavenumber $\gamma$. Labels $(a)$–$(g)$ designate points of interest

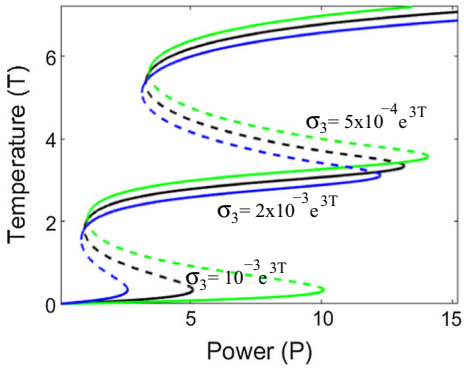


**Fig. 10** Response of Double-S-curve as $A_3$ is varied

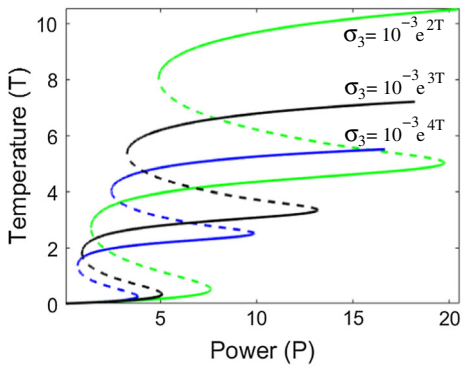


**Fig. 11** Response of Double-S-curve as $b_3$ is varied

at the adjacent resonance state, as shown by **e** and **f**. Finally there are other locations, such as **g**, where turning point remains the same across adjacent resonant states.

The set of thermal parameters are studied by graphing the power response for different values of a chosen parameter. We find this presentation to more instructive than by plotting the parametric curves. Initially we consider the characterization of the inner layer loss factor parameters $A_3$ and $b_3$. Figure 10 shows three power response curves as $A_3$ is increased. As expected from Eq. (21), decreasing the parameter increases the power, since $P \sim \frac{1}{A_3}$. We also notice a slight increase in temperature as well. The response that occurs by varying $b_2$, depicted in Fig. 11, appears to be in scaling the entire Double-S-curve. Temperature and power are decreased with the increasing values of $b_2$ yielding what appears to be a smaller version of the same Double-S-curve. Applying Eq. (21) for $b_2 = 2$ and 3 yields

$$P_1 = \frac{2\mathcal{L}(T)}{10^{-3}\mathrm{e}^{2T}\|E_3\|_2^2(T)} = \mathrm{e}^T \frac{2\mathcal{L}(T)}{10^{-3}\mathrm{e}^{3T}\|E_3\|_2^2(T)} = \mathrm{e}^T P_2, \tag{28}$$

which shows the power level is scaled exponentially with temperature.

We continue by considering, for the first time, the absorption of EM energy within all three layers of the laminate. Thus, this requires the use of Eq. (27) as the equation for the power response curve. The characterization of the outer layer loss factor parameters $A_2$ and $b_2$ are presented. Starting with $A_2$, four power response curves are plotted in Fig. 12. The black curve is the lossless case. The next three graphs show a decrease in the temperature of branch E as $A_2$ increases. Alternatively, we can strengthen the loss factor by increasing the exponent parameter $b_2$ instead, shown in Fig. 13. It demonstrates that, as the exponential increases, the top branch actually lowers in temperature

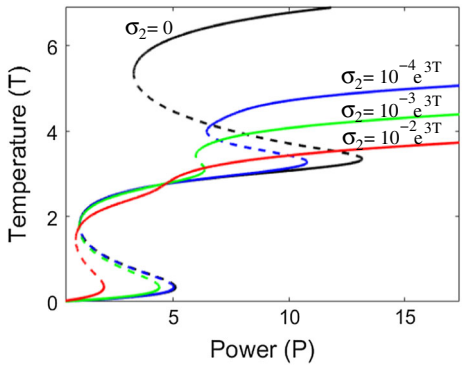


**Fig. 12** Response of Double-S-curve as $A_2$ is varied

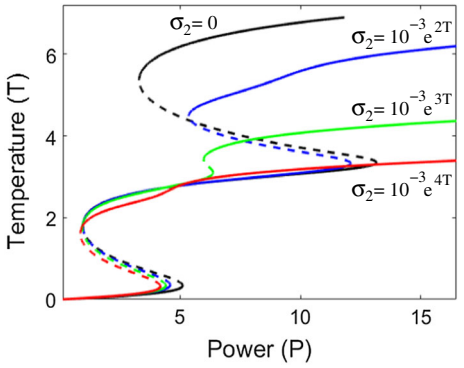


**Fig. 13** Response of Double-S-curve as $b_2$ is varied

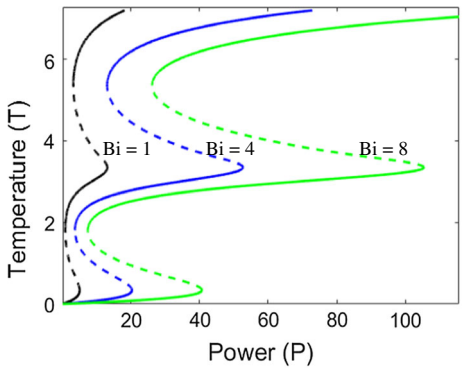


**Fig. 14** Response of Double-S-curve as $Bi$ is varied

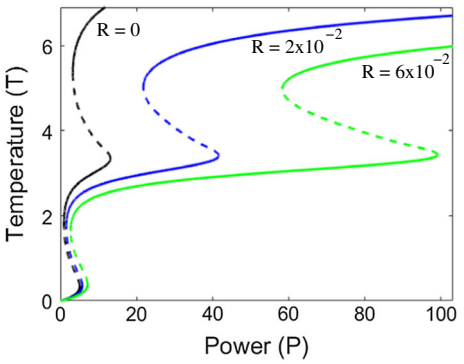


**Fig. 15** Response of Double-S-curve as $R$ is varied

to merge with the middle branch. This leads to the question that if very lossy outer layers yield an S-curve, where the top branch is at temperatures for safe and efficient operation, would a heat exchanger with mirrored properties be more efficient? A heat exchanger has lossy solid dielectric as the outer layers and the lossless fluid as the inner layer.

The two remaining parameters to be characterized are the Biot number and radiation parameter, which model the heat lost to the environment. They are responsible for the energy balance, which establishes the steady states of the system, and thus play a critical part in how each of the branches of the Double-S-curve behave.

Figure 14 graphs the power response when $Bi = 1, 4, 8$. It shows that the temperature of the turning points remain constant while the power increases linearly with Biot number. This is significant. Since the Biot number defines how much energy is lost to the environment through external advection, by artificially increasing the external advection, the power range for which the middle branch is accessible increases. A large power range is desirable because it would better ensure that small fluctuations in power would not move the temperature off the branch. The ability to change this parameter during operation makes it a useful mechanism in controlling the EM heating and the dangerous effects of thermal runaway.

The radiation parameter is similar to the Biot number except that with a higher radiation number the quartic dependence of the temperature on power becomes apparent. It also has the ability to create a large power range for the middle layer, however, blackbody radiation is intrinsic to a material and thus cannot be used during operation to aid in heating control (Fig. 15).

The middle branch has therefore been shown to be a new way of avoiding thermal runaway and the dangerous effects of the high temperatures associated with the top branch. It also provides more efficient heating than the

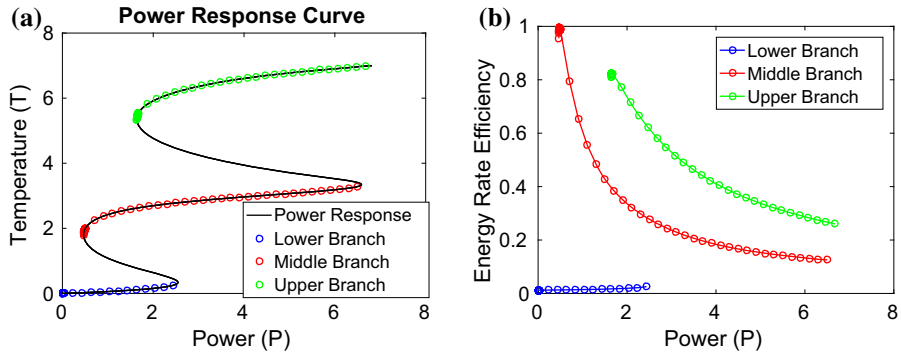


**Fig. 16** Double-S-curve showing position of markers used to plot the efficiency for the rate of energy absorption (**a**). Efficiency for the rate of energy absorption in each of the three stable branches (**b**)

alternative lower branch. The efficiency of a heat exchanger is vital to its overall utility as a viable means of energy collection. The efficiency of how EM energy is transferred to thermal energy is denoted $\mathcal{E}_{\mathrm{AB}}$. The rate energy is absorbed by the EM radiation is $P\sigma_3(T)\|E_3\|_2^2$. Setting the temperature derivative equal to zero, gives a simple relation for the maximum energy rate,

$$-\frac{1}{\|E_3\|_2^2}\frac{\partial\|E_3\|_2^2}{\partial T} = b_3. \tag{29}$$

This can be closely related to the location of the turning points for the power response, which can be found by setting the temperature derivative of $\ln(P)$ to zero,

$$-\frac{1}{\|E_3\|_2^2}\frac{\partial\|E_3\|_2^2}{\partial T} = b_3 - \frac{\partial(\ln\mathcal{L})}{\partial T}. \tag{30}$$

Since the losses $\mathcal{L}(T)$ are polynomial in temperature while $\sigma_3(T)$ and $\|E_3\|_2^2$ are exponential at higher temperatures, $\frac{\partial(\ln\mathcal{L})}{\partial T}$ is small, hence we expect the maximum energy absorption to occur near the left turning points. This is confirmed by Fig. 16 showing the absorbed efficiency for each branch. There are two left turning points in an Double-S-curve. Figure 16 shows the middle branch can be even more efficient than the upper branch despite having a lower operating temperature.

Though the maximum efficiency occurs at the low-power regions of the turning points, it is also the first location of the nonexistence regions once diffusion in $x$ is considered. As shown in the following section, the greater the thermal conductivity the less is the efficiency that can be achieved.

## 3 Thin domain asymptotics: nonuniform heating

The previous section reviews the existence of a Double-S-curve [19] and describes the implications of it in more detail. In addition, the model assumes uniform heating in $x$ on the infinite domain $x \in (-\infty, \infty)$, or, equivalently, on a finite domain $x \in [0, L]$ with zero flux boundary conditions. In this section, we consider the domain to be finite, as shown by Fig. 17, and relax the uniform heating assumption by applying a Dirichlet condition at one boundary and a zero flux condition at the other. The governing equation is then given by Eq. (19) with boundary conditions (12)–(15),

$$T = 0, \quad x = 0, \tag{31}$$

$$\frac{\partial T}{\partial x} = 0, \quad x = L. \tag{32}$$

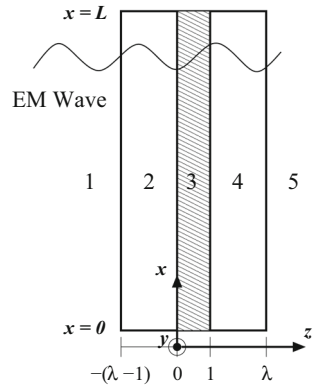


**Fig. 17** Finite domain triple-layer laminate

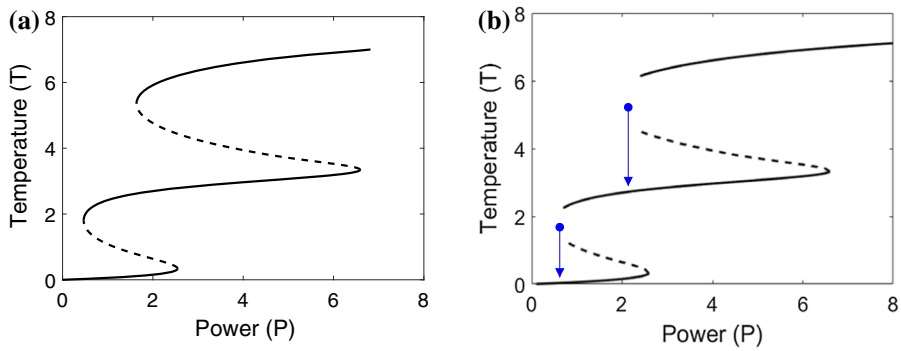


**Fig. 18** Power response of Eq. (20) for uniform heating in $x$ (**a**), power response of Eq. (19) for nonuniform heating in $x$ with $\bar{k} = 0.5$. Nonexistence regions where steady states cease appear near the left two turning points. Blue arrows show how temperature decreases within the nonexistence regions (**b**). Other parameters used to produce these curves include $\epsilon_2 = \left(\frac{7\pi}{2}\right)^2$, $\epsilon_3 = \pi^2$, $\gamma = 1$, $K = 0.5$, $Bi = 0.5$, $Q = 0$, $\sigma_3(T) = 10^{-3}\mathrm{e}^{3T}$. (Color figure online)

and initial condition (17). Physically, this models a thin three-layer laminate exposed to cold reservoir at $x = 0$ and sufficiently long enough for the material to heat up at the other boundary allowing the zero flux condition to be valid.

By requiring that the channel length is long enough so that Eq. (32) is valid, we can define a power response curve for the steady-state solution $T(x)$ as

$$P = \frac{2\mathcal{L}(T(L))}{\sigma_3(T(L))\|E_3\|_2^2(T(L))}. \tag{33}$$

We are interested in how the power response curve changes as the diffusive transport change the heating effects. Figure 18a shows the power response for the uniform heating case while Fig. 18b shows the power response curve when diffusive effects are considered. Increasing the thermal conductivity produces regions where steady-state solutions cease to exist. At these low power levels, the temperature no longer has steady states and decreases until it reaches a lower stable state.

We solve Eq. (19) for transient solutions with an Implicit–Explicit (IMEX) numerical scheme. The Crank–Nicolson is applied to the linear terms, and Adams–Bashforth is used on the nonlinear source term. It was chosen as a first attempt at a solution, however, there are more stable IMEX methods [34]. Figure 19 examines the behavior of solutions within a nonexistence region. It shows the resulting solution when the initial temperature is $T(0, x) = 7$. We note that the temperature decreases over time and moves as a traveling wave until the temperature at $x = L$ reaches the stable temperature of the middle branch. We prove that traveling-wave solutions exist, then develop

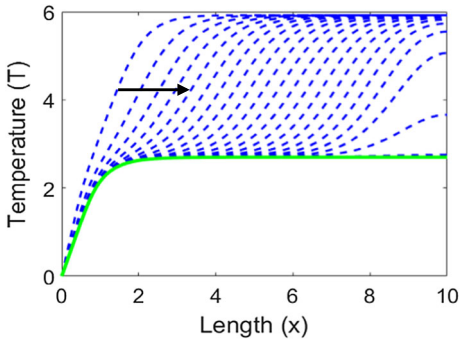


**Fig. 19** (Blue-dashed) transient solution solving Eq. (19) subject to Eqs. (31)–(32) at every 2.5 s for $\overline{k} = 0.5$ and $P = 2$. Arrow shows direction traveling wave propagates. (Green-solid) steady-state solution. (Color figure online)

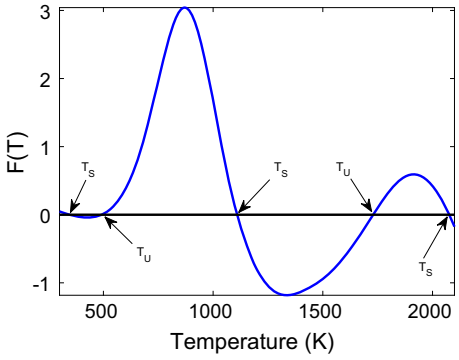


**Fig. 20** Example of the source/loss term $F(T)$ for $P = 2$, $\sigma_3(T) = 10^{-3}e^{3T}$, $\epsilon_2 = \left(\frac{7\pi}{2}\right)^2$, $\epsilon_3 = \pi^2$, $Bi = 0.5$, $Q = 0$. It shows two distinct intervals that exhibit bistability

approximations for the wave velocity and the power level separating traveling-wave solutions from steady-state solutions.

**Theorem 1** *Equation* (19) *has traveling wave solutions when* $\overline{k} > 0$.

*Proof* Let $T_{S1}$ and $T_{S2}$ denote two stable steady-state temperatures and $T_U$ denote the unstable steady state at the outlet $x = L$, such that $T_{S1} < T_U < T_{S2}$. We intend to show traveling-wave solutions exist between the two stable temperatures. Since there is the possibility of two such sets of steady-state temperatures for the Double-S-curve power response, there exist two sets of traveling wave solutions. The solutions are monotonically increasing. Transforming Eq. (19) to the moving reference frame, let $w = x - vt$, so

$$\overline{k}\frac{\partial^2 T}{\partial w^2} + v\overline{\rho c_p}\frac{\partial T}{\partial w} + P\sigma_3(T)\|E_3\|_2^2(T) - 2\mathcal{L}(T) = 0. \tag{34}$$

We further make the transformation $\widetilde{w} = -w/\sqrt{\overline{k}}$. The negative sign is adopted in order to force the solution to be monotonically decreasing which is used in the existence theorem. Furthermore, the scaling on $\sqrt{\overline{k}}$ is to group all the coefficients together. The resulting equation becomes

$$\frac{\partial^2 T}{\partial \widetilde{w}^2} + c\frac{\partial T}{\partial \widetilde{w}} + F(T) = 0, \tag{35}$$

where $c = -v\overline{\rho c_p}/\sqrt{\overline{k}}$ and $F(T) = P\sigma_3(T)\|E_3\|_2^2(T) - 2\mathcal{L}(T)$. The far field conditions are then given by $\lim_{\widetilde{w}=\infty} T = T_{S1}$ and $\lim_{\widetilde{w}=-\infty} T = T_{S2}$. The source term, an example of which is shown in Fig. 20, exhibits bistability between the low and high temperatures. Bistability holds if $F(T) \leq 0$ in a right half neighborhood of $T_{S1}$ and $F(T) \geq 0$ in a left half neighborhood of $T_{S2}$.

The remainder of the proof follows from Theorem 1.5 of Chap. 4 in [35]. We separate Eq. (35) into the first-order system

$$T' = q, \tag{36}$$

$$q' = -cq - F(T). \tag{37}$$

Solutions to Eq. (35) satisfying the far field conditions correspond to phase plane trajectories connecting stationary points $(T_{S1}, 0)$ and $(T_{S2}, 0)$. Suppose $c = 0$. Let $(T, q_1^0(T))$ be the trajectory approaching the stationary point $(T_{S1}, 0)$ and $(T, q_2^0(T))$ be the trajectory leaving stationary point $(T_{S2}, 0)$. Then $q_1^0(T_{S1}) = 0$, $q_1^0(T_U) < 0$, $q_2^0(T_{S2}) = 0$, and $q_2^0(T_U) < 0$ hold from the bistability of $F(T)$. If $q_1^0(T_U) = q_2^0(T_U)$, the trajectories coincide connecting the two stationary points, thus the theorem is proved.

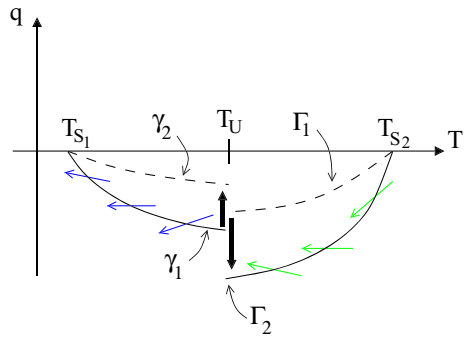


**Fig. 21** Phase diagram depicting proof of traveling wave solutions, which exist provided curves $\gamma$ and $\Gamma$ vary continuously with wave speed $c$ and intersect at $T_U$ for some $c$

Suppose then that $q_1^0(T_U) \neq q_2^0(T_U)$. Consider a family of trajectories $\gamma_i := (T, q_1^{c_i}(T))$ and $\Gamma_i := (T, q_2^{c_i}(T))$ for $c \neq 0$, where $q_1^c(T_{S1}) = q_2^c(T_{S2}) = 0\ \forall c$. Next, we prove that $q_1^c$ ($q_2^c$) is monotonically decreasing (increasing) with respect to $c$. Let $c_1 > c_2$ and divide through Eq. (37) by $q$; substituting in Eq. (36), we have that

$$\frac{\mathrm{d}q_j}{\mathrm{d}T} = -c - \frac{F(T)}{q_j^c}. \tag{38}$$

From this, we can conclude that

$$\left.\frac{\mathrm{d}q_1}{\mathrm{d}T}\right|_{c=c_1,\gamma=\gamma_1} < \left.\frac{\mathrm{d}q_1}{\mathrm{d}T}\right|_{c=c_2,\gamma=\gamma_1}, \tag{39}$$

$$\left.\frac{\mathrm{d}q_2}{\mathrm{d}T}\right|_{c=c_1,\gamma=\gamma_2} < \left.\frac{\mathrm{d}q_2}{\mathrm{d}T}\right|_{c=c_2,\gamma=\gamma_2}. \tag{40}$$

These inequalities are visualized in Fig. 21. $\left.\frac{\mathrm{d}q_1}{\mathrm{d}T}\right|_{c=c_1,\gamma=\gamma_1}$ is given by the slope of $\gamma_1$, while $\left.\frac{\mathrm{d}q_1}{\mathrm{d}T}\right|_{c=c_2,\gamma=\gamma_1}$ is given by the slope of the blue vectors (vectors left of $T_U$). $\left.\frac{\mathrm{d}q_2}{\mathrm{d}T}\right|_{c=c_2,\Gamma=\Gamma_2}$ is given by the slope of $\Gamma_2$, while $\left.\frac{\mathrm{d}q_2}{\mathrm{d}T}\right|_{c=c_1,\gamma=\gamma_2}$ is given by the slope of the green vectors (vectors right of $T_U$). Equation (39) implies that $\gamma_2$ lies above $\gamma_1$, otherwise since both curves intersect at $(T_{S1}, 0)$, if curve $\gamma_2$ was below $\gamma_1$, then they could intersect a second time based on the trajectories of the system with $c_2$ along $\gamma_1$ (blue vectors). Similarly, Eq. (40) implies that $\Gamma_1$ lies above $\Gamma_2$, otherwise, since both curves intersect at $(T_{S2}, 0)$, if curve $\Gamma_1$ was below $\Gamma_2$ then it could intersect a second time based on the trajectories of the system with $c_1$ along $\Gamma_2$ (green vectors). Therefore, $q_1^{c_1} < q_1^{c_2}$ on $T \in [T_{S1}, T_U]$ and $q_2^{c_1} > q_2^{c_2}$ on $T \in [T_U, T_{S2}]$, so $q_1^c$ ($q_2^c$) is monotonically decreasing (increasing) with respect to $c$.

Next, we show that $q_j^c$ is continuous with respect to $c$ in the uniform norm. Let $\varepsilon > 0$. Choose $\delta = \frac{\varepsilon}{T_{\max}}$, where $T_{\max} = T_U$ for $q_1$ on $T \in [T_{S1}, T_U]$ and $T_{\max} = T_{S2}$ for $q_2$ on $T \in [T_U, T_{S2}]$. The difference of (37) evaluated along $\gamma_1$ and $\gamma_2$ yields

$$q'\big|_{\gamma_1} - q'\big|_{\gamma_2} = -c\ T'\big|_{\gamma_1} + c_0\ T'\big|_{\gamma_2}, \tag{41}$$

where Eq. (36) was substituted for $q$. Integrating both sides and taking the uniform norm results in $\|q^c - q^{c_0}\|_\infty = |c - c_0|\|T\|_\infty < \delta T_{\max} = \varepsilon$. Therefore, the two trajectories $q_1^c$ and $q_2^c$ are continuous with respect to $c$.

Finally, suppose that $q_1^0(T_U) > q_2^0(T_U)$; then by increasing $c$ from zero, $q_1^c(T_U)$ decreases while $q_2^c(T_U)$ increases and since they are continuous in $c$, there must exist a $c$ such that $q_1^c(T_U) = q_2^c(T_U)$. Suppose instead, that $q_1^0(T_U) < q_2^0(T_U)$; then we find equality by decreasing $c$ from zero. This implies a trajectory connects the two stationary points, therefore, a wave solution exists. □

Now that we know such traveling-wave solutions exist, we derive expressions for the wave velocity $v$. We employ the narrow reaction zone (NRZ) method first developed as an approximation to the speed of flame propagation [36].

The main assumption is that the reaction zone, which in this case is the thermal runaway event, occurs only on a narrow domain. In this context, the reaction is the heat source from microwave absorption which occurs everywhere on the domain. However, since the source is much stronger at the thermal runaway event than at other locations in the domain, it possesses similar characteristics as a NRZ. The approximate equations presented in the NRZ method in [35] are obtained rigorously as asymptotic solutions in boundary layer theory.

We begin the analysis by scaling Eq. (35). Let $\widetilde{w} = \varepsilon^d r$, and $F(T) = \delta \widehat{F}(T)$, where $\varepsilon, \delta \ll 1$. The scaled equation becomes

$$\varepsilon^{-2d} \frac{\partial^2 T}{\partial r^2} + \varepsilon^{-d} c \frac{\partial T}{\partial r} + \delta \widehat{F}(T) = 0. \tag{42}$$

The boundary layer theory requires we find the dominant balance between the terms. The first balance we consider is that of the second and third terms, which implies that $\delta = \varepsilon^{-d_1} c$. Consistency requires $\delta = \varepsilon^{-d_1} c \gg \varepsilon^{-2d_1}$, which implies that $c \gg \varepsilon^{-d_1}$. The equation for this balance becomes

$$c \frac{\partial T}{\partial r} + \widehat{F}(T) = 0 \quad \text{(outer layer)}. \tag{43}$$

The second balance is for the first and second terms, where $\varepsilon^{-2d_2} = \varepsilon^{-d_2} c$, which means that $c = \varepsilon^{-d_2}$. In order to be consistent, it must be that $\delta \ll \varepsilon^{-2d_2}$. The resulting equation is then

$$\frac{\partial^2 T}{\partial r^2} + c \frac{\partial T}{\partial r} = 0 \quad \text{(middle layer)}. \tag{44}$$

The final balance we consider is of the first and third terms, so that $\varepsilon^{-2d_3} = \delta$. To be consistent, it further requires that $\delta = \varepsilon^{-2d_3} \gg \varepsilon^{-d_3} c$, which implies that $c \ll \varepsilon^{-d_3}$. Then the governing equation in this region is

$$\frac{\partial^2 T}{\partial r^2} + \widehat{F}(T) = 0 \quad \text{(inner layer)}. \tag{45}$$

All three of these balances can be consistent if the scales for each region are chosen such that $\varepsilon^{-d_1} \ll c = \varepsilon^{-d_2} \ll \varepsilon^{-d_3}$, which implies that $d_3 < d_2 < d_1$. This provides the order of the nested layers with boundary layer thickness of the regions given by $\varepsilon^{d_3} \ll \varepsilon^{d_2} \ll \varepsilon^{d_1}$.

An analysis of the outer-most region shows it is equivalent to the steady-state constant solutions. It should be clear that solutions $T(r) \equiv T_{S2}$ and $T(r) \equiv T_{S1}$ satisfy Eq. (43). Attempting to find a non-constant solution, we apply separation of variables to Eq. (43) producing two implicit solutions in this outer most region of the form:

$$\int_T^{T_{S2}} \frac{c}{\widehat{F}(T)} \, \mathrm{d}T = -r, \quad \lim_{r \to -\infty} T = T_{S2}, \tag{46}$$

$$\int_{T_{S1}}^{T} \frac{c}{\widehat{F}(T)} \, \mathrm{d}T = -r, \quad \lim_{r \to \infty} T = T_{S1}. \tag{47}$$

The integrands are singular since $\widehat{F}(T_{S2}) = \widehat{F}(T_{S1}) = 0$. Since $T_{S2}$ and $T_{S1}$ are simple roots, $\widehat{F}(T)$ approaches the zeros linearly, as shown in Fig. 20; the integrals diverge for all temperatures $T$. Therefore, the only solutions to (43) are the constant solutions.

The main assumption in applying the NRZ method is that the reaction zone is very small, which is to take the limit as $\varepsilon^{d_3} \to 0$. In this limit, the matching conditions required to complete the boundary layer theory are to match the two outer solutions together, instead of matching to the inner solution as with the standard method of matched asymptotics.

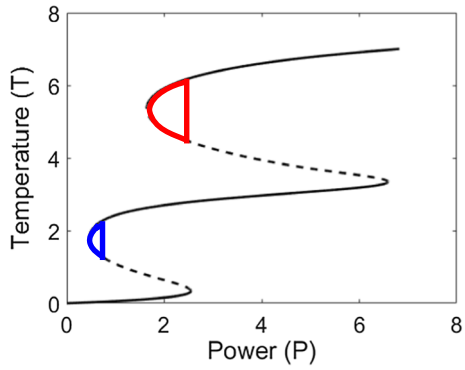


**Fig. 22** Power response for $\overline{k} = 0.5$, where highlighted regions possess traveling wave solutions and no steady states

We find the solution to Eq. (44) by separation of variables. The solutions depend on the sign of $c$. Applying the narrow reaction approximation, we match the two solutions of the outer regions together. The solutions for $c \leq 0$ are

$$T = \begin{cases} T_{S1}, & w \in (-\infty, 0), \\ T_{S2} - (T_{S2} - T_{S1})\mathrm{e}^{-\frac{v\overline{\rho c_p}}{\overline{k}}w}, & w \in (0, \infty), \end{cases} \tag{48}$$

and the solutions when $c \geq 0$ are

$$T = \begin{cases} T_{S1} + (T_{S2} - T_{S1})\mathrm{e}^{-\frac{v\overline{\rho c_p}}{\overline{k}}w}, & w \in (-\infty, 0), \\ T_{S2}, & w \in (0, \infty). \end{cases} \tag{49}$$

Next, we integrate Eq. (45) in terms of $r$ from $(-\infty, \infty)$. In terms of $w$, it yields the jump condition

$$\frac{\overline{k}}{2}\left[\left(\frac{\partial T}{\partial w}\right)^2\bigg|_{0+} - \left(\frac{\partial T}{\partial w}\right)^2\bigg|_{0-}\right] = -\int_{T_{S1}}^{T_{S2}} F(T)\,\mathrm{d}T. \tag{50}$$

Matching the middle solution to the inner solution and solving for $v$, gives the approximation for the wave velocity

$$v = \sqrt{-\frac{2\overline{k}}{\overline{\rho c_p}^2(T_{S2} - T_{S1})^2}\int_{T_{S1}}^{T_{S2}} F(T)\,\mathrm{d}T}, \quad v \geq 0, \tag{51}$$

where the integral over $F(T)$ is negative. This approximation to the wave velocity can be used to approximate the power level separating the regions of traveling-wave solutions from the steady-state solutions in the power response curve. The IMEX numerical solution plotted in Fig. 19 shows that traveling-wave solutions occur in the nonexistence regions. Figure 22 highlights the regions where steady states have ceased to exist. Figure 23 shows how the wave velocity decreases, as $P$ increases, within these nonexistence regions. The wave velocity predicted by the NRZ method and calculated by the IMEX method is zero at the transition power. Hence, by setting Eq. (51) equal to zero we obtain an approximate condition for the power $P$ at which traveling-wave solutions transition to steady-state solutions.

## 4 Direct numerical solution

We validate the previous asymptotic analysis by implementing a full numerical solution of Eqs. (9)–(17) for a comparison. Each of the three domains are discretized according to the PR-ADI method using spatial steps

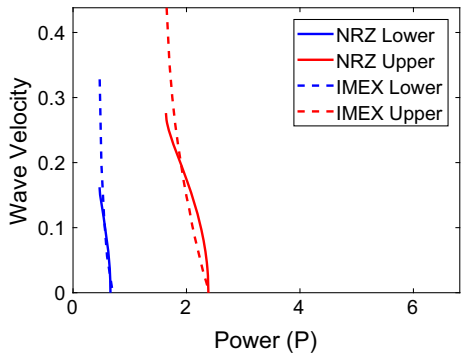


**Fig. 23** Wave velocity predicted by the NRZ method and calculated by the IMEX simulation

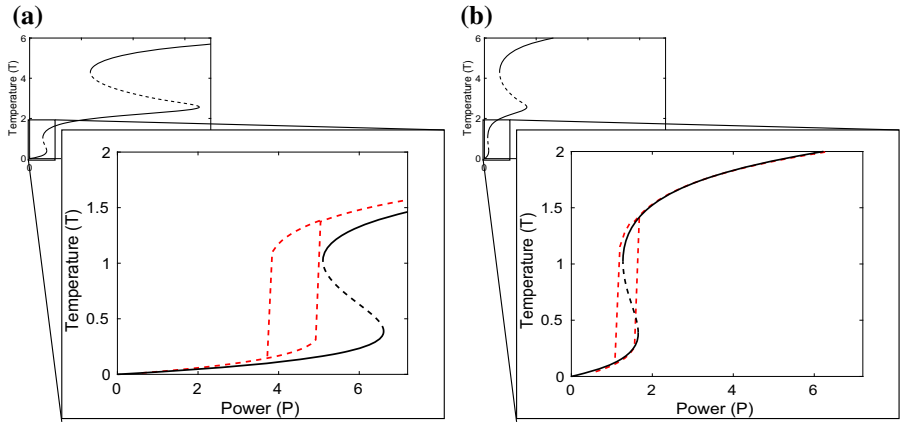


**Fig. 24** Power response curves of the first hysteresis of a Double-S-curve when $Bi = 0.5$ (**a**) and $Bi = 0.125$ (**b**). The black line depicts stable (solid) and unstable (dashed) branches of the power response according to the asymptotic model. The power response from the PR-ADI method is shown by the red-dashed line. (Color figure online)

$\Delta x = 0.05$, $\Delta y = 0.1$, a time step of $\Delta t = 0.1$, and a convergence tolerance of $10^{-5}$. The external boundary conditions involving derivatives are solved with central differencing with ghost points, while the internal boundaries are discretized with first order differencing for the continuity and continuity of flux. The electric field is solved exactly using the Helmholtz equation which assumes permittivity gradients are negligible. The average temperature in region 3 is plotted for the asymptotic model and PR-ADI method in Fig. 24a using $Bi = 0.5$ and Fig. 24b using $Bi = 0.125$.

Typical run times to generate the power response from the PR-ADI method are around 10 h using eight nodes employing the MATLAB Parallel Computing Toolbox on a local HPC cluster. These figures demonstrate the importance of spatial information in the spanwise direction. When the spanwise spatial variation is large, $Bi = 0.5$, according to the PR-ADI the hysteresis occurs at similar temperatures, but at lower powers than those predicted by the asymptotic model. The PR-ADI method reveals that thermal runaway is initiated locally, when a particular point in space achieves a critical temperature. This inherently requires less power than the asymptotic model which initiates thermal runaway when the average spanwise temperature, which was modeled as being uniform in $z$, achieves the critical temperature. When spanwise spatial variation is less, $Bi = 0.125$, the average temperature gradient decreases, making the spanwise temperature more uniform. Hence, the thin domain assumption used in the asymptotics, that temperature was independent of $z$, is also valid for PR-ADI model. This result validates the asymptotic model and corroborates a COMSOL model solving Eqs. (9)–(17) presented by [23] who compares their results to the asymptotic model of [19]. The spatial dependence in the 2D COMSOL model generated a hysteresis

in the power response curve at similar power levels as those predicted by the PR-ADI method [23], along with the trend for better agreement as $Bi$ is decreased.

## 5 Conclusions

It has been demonstrated that by tuning the frequency, permittivity and width of a triple-layer laminate, the resulting Bragg resonance causes a new steady state for EM heating in the form of the Double-S-curve. This previously unknown branch of steady states is established through the rapid attenuation of EM energy from within the lossy material. The range of temperatures over which the steady states are generated make it ideal for high-temperature ceramic heating, where the temperatures are high enough to be efficient and useful, yet low enough where the compromising effects of thermal stress, melting, or sublimation are avoided. A significant difficulty in producing the resonance during EM heating needs to be mentioned. The asymptotic method presented in this paper assumes the real part of the dielectric constant, which is required to produce the resonance, to be a constant. It is known that this parameter is dependent on temperature. This dependency may detune the field away from the resonant mode as temperature increases due to heating. It should also be mentioned that for beamed energy applications the operator would have real-time control of the incident wave frequency which could be altered with the temperature increase to remain at resonance.

The efficiency at which energy is absorbed is presented for each branch, where maximum efficiency occurs at the left turning points. The steady-state solutions become nonexistent at the left turning points in the presence of the Dirichlet condition and recede as the thermal conductivity increases. The steady states are replaced by traveling wave solutions which force the higher temperature down the length of the layer until the temperature comes to rest at a lower branch on the Double-S-curve. The knowledge that left turning points possess the greatest efficiency, but are the first to become nonexistent under diffusive effects, requires the application of an optimization analysis. Such an optimization would determine the efficiency at which energy is removed from the system, which is the most effective at high thermal conductivity, where solutions do not exist.

An analytical estimation of the wave velocity was determined for the traveling wave solutions by applying the NRZ method and compared against the velocity determined from the diffusion equation using the IMEX method. The power level associated with the location of the interface between traveling wave and steady-state solution is then able to be estimated by setting the wave velocity to zero.

The asymptotic method used to produce the Double-S-curve for uniform heating was validated by comparing it to a PR-ADI scheme. This agrees with similar findings by [23] that spanwise spatial variations affect the material heating when external losses are large but becomes comparable to the asymptotic model with low losses. Model validation strengthens the prediction that the Double-S-curve can be utilized to help control the nonlinear effects of EM heating.

The natural extension to the problem of multiple layers is of particular interest. Bragg resonance cavities will usually employ multiple layers as the alternation of high permittivity layers and low permittivity layers increases the quality of the resonator. Additionally scenarios that include more than one lossy defect layer pose the possibility of unique heating behavior. The energy absorption in each layer are coupled together where the energy absorption in one layer effects the field and thus the energy absorption in the other layers. As mentioned previously, a layered medium may also be engineered with multiple defects specifically designed to induce resonance in a single defect at different temperatures. The expanse of possible discoveries is sure to prompt many avenues of further research, which will be required if the full extent of this possible technology is to be realized.

**Acknowledgements** The authors are grateful for the support from the Air Force Office of Scientific Research; Award FA9550-15-0476 and the National Science Foundation MRI Grant DMS-1337943 for high performance computing. This work was funded by AFOSR Award FA9550-15-0476 and NSF MRI Grant DMS-1337943 for high performance computing.

## A Closure argument for effective energy equation

Here we describe briefly the argument to derive the effective energy equation (19). Since $T_j^{(0)} = T^{(0)}(t,x)$ at leading order, we need to consider the problem (9)–(15) at $O(\eta^2)$. This results in the following problems for $T_j^{(2)}$,

$$\alpha \frac{\partial^2 T_2^{(2)}}{\partial z^2} = \left\{ \frac{\partial T^{(0)}}{\partial t} - \alpha \frac{\partial^2 T^{(0)}}{\partial x^2} \right\}, \tag{52}$$

$$\frac{\partial^2 T_3^{(2)}}{\partial z^2} = \left\{ \frac{\partial T^{(0)}}{\partial t} - \frac{\partial^2 T^{(0)}}{\partial x^2} - P\sigma_3(T^{(0)})\,|E_e|^2 \right\}, \tag{53}$$

$$\alpha \frac{\partial^2 T_4^{(2)}}{\partial z^2} = \left\{ \frac{\partial T^{(0)}}{\partial t} - \alpha \frac{\partial^2 T^{(0)}}{\partial x^2} \right\}, \tag{54}$$

subject to the boundary conditions

$$K \frac{\partial T_2^{(2)}}{\partial z} = Bi\, T^{(0)} + R\left[ (T^{(0)}+1)^4 - 1 \right], \quad z = -(\lambda - 1), \tag{55}$$

$$T_2^{(2)} = T_3^{(2)}, \quad K \frac{\partial T_2^{(2)}}{\partial z} = \frac{\partial T_3^{(2)}}{\partial z}, \quad z = 0, \tag{56}$$

$$T_3^{(2)} = T_4^{(2)}, \quad \frac{\partial T_3^{(2)}}{\partial z} = K \frac{\partial T_4^{(2)}}{\partial z}, \quad z = 1, \tag{57}$$

$$-K \frac{\partial T_4^{(2)}}{\partial z} = Bi\, T^{(0)} + R\left[ (T^{(0)}+1)^4 - 1 \right], \quad z = \lambda. \tag{58}$$

To find Eq. (19), we integrate Eq. (52) over $-(\lambda - 1) < z < 0$, Eq. (53) over $0 < z < 1$, and Eq. (54) over $1 < z < \lambda$. Applying the boundary conditions (55)–(58) results in the Eq. (19).

## B Exponential electrical conductivity

There have been many proposals of functional forms describing the temperature dependence of the dielectric loss $\epsilon''$ or the electrical conductivity $\sigma_3$ [37]. It is the case that many dielectric materials possess an exponential dependence with temperature. Figure 25 shows the curve fitting of data to the form $\epsilon''(T) = A_3 e^{b_3 T}$, where $T$ is the temperature and parameters $A_3$ and $b_3$ are found by the curve fitting. In both of these examples there is good agreement with the exponential dependence on temperature.

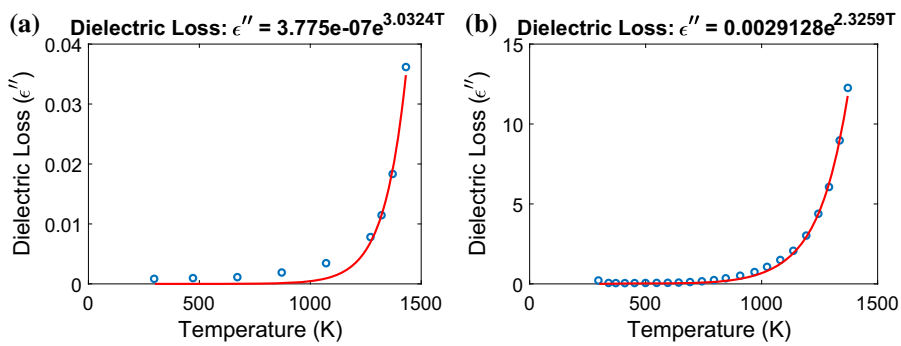


**Fig. 25** Least squares curve fitting to data taken from [26] on the dielectric loss of silicon dioxide (**a**), and least squares curve fitting to data taken from [18] on the effective dielectric loss of zirconia (**b**)

## References


1. Datta AK, Anantheswaran RC (2001) Handbook of microwave technology for food applications. CRC Press, New York
2. Leadbeater N (2010) Microwave heating as a tool for sustainable chemistry. In: Cann MC (ed) Sustainability: contributions through science and technology. CRC Press, Boca Raton
3. Aguilar-Garib J (2011) Chap. 12: thermal microwave processing of materials. In: Grundas C (ed) Advances in induction and microwave heating of mineral and organic materials. InTech, Rijeka, pp 243–268
4. Chandrasekaran S, Ramanathan S, Basak T (2012) Microwave materials processing–a review. AlChE J 58(2):330–363
5. Singh S, Gupra D, Jain V, Sharma A (2015) Microwave processing and applications of manufacturing industry: a review. Mater Manuf Process 30(1):1–29
6. Willert-Porada M (2006) Advances in microwave and radio frequency proceedings. Springer, Berlin
7. Jamar A, Majid Z, Azmi W, Norhafana M, Razak A (2016) A review of water heating system for solar energy applications. Int Commun Heat Mass Transf 76:178–187
8. George P, Beach R (2012) Beamed-energy propulsion (BEP) study. Technical report, NASA/TM-2012-217014
9. Kriegsmann G (1992) Thermal runaway in microwave heated ceramics: a one-dimensional model. J Appl Phys 71(4):1960–1966
10. Pelesko J, Kriegsmann G (1997) Microwave heating of ceramic laminates. J Eng Math 32:1–18
11. Osepchuck J (1984) A history of microwave heating applications. IEEE Trans Microw Theory Tech 32:1200–1224
12. Chandran M, Neculaes V, Brisco D, Katz S, Schoonover J, Cretegny L (2013) Experimental and numerical studies of microwave power redistribution during thermal runaway. J Appl Phys 114:204904
13. ChangJun L, Sheen D (2008) Analysis and control of the thermal runaway of ceramic slab under microwave heating. Sci China E 51(12):2233–2241
14. Liu C, Sheen D (2008) Analysis and control of the thermal runaway of ceramic slab under microwave heating. Sci China E 51:2233–22415
15. Parris P, Kenkre V (1997) Thermal runaway in ceramics arising from the temperature dependence of the thermal conductivity. Phys Status Solidi (b) 200:1–9
16. Semenov V, Zharova N (2006) Thermal runaway and hot spots under controlled microwave heating. In: Advances in microwave radio frequency processing, p 482–490
17. Vriezinga C, Sánchez-Pedreño S, Grasman J (2002) Thermal runaway in microwave heating: a mathematical analysis. Appl Math Model 26:1029–1038
18. Yakovlev V, Allan S, Fall M, Shulman H (2011) Computational study of thermal runaway in microwave processing of zirconia. In: Tao J (ed) Microwave and RF power applications. Cépaduès Éditions, Toulouse, pp 303–306
19. Gaone J, Tilley B, Yakovlev V (2017) Permittivity-based control of thermal runaway in a triple-layer laminate. In: IEEE MTT-S international microwave symposium digest, Honolulu, HI, June 2017. ISBN 978-1-5090-6360-4
20. Kriegsmann G (1992) Thermal runaway and its control in microwave heated ceramics. MRS Proc 269:257
21. Wu X, Thomas J, Davis W (2002) Control of thermal runaway in microwave resonant cavities. J Appl Phys 92(6):3374–3380
22. Kriegsmann G, Brodwin M, Watters D (1990) Microwave heating of a ceramic halfspace. SIAM J Appl Math 50(4):1088–1098
23. Mohekar A, Gaone J, Tilley B, Yakovelev V (2018) Multiphysics simulation of temperature profiles in a triple-layer model of a microwave heat exchanger. In: IEEE MTT-S international microwave symposium digest, Philadelphia, PA, June 2018. ISBN 978-1-5386-5067-7
24. Griffiths D (1999) Introduction to electrodynamics. Pearson Education, Upper Saddle River
25. Jackson J (1999) Classical electrodynamics. Wiley, New York
26. Westphal W, Sils A (1972) Dielectric constant and loss data. Technical Report AFML-TR-72-39. Air Force Materials Laboratory
27. Rayleigh L (1888) On the remarkable phenomenon of crystalline reflexion described by Prof. Stokes. Philos Mag 26(160):256–265
28. Ozbay E, Temelkuran B, Bayindir M (2003) Microwave applications of photonic crystals. Prog Electromagn Res 41:185–209
29. Vovchenko L, Lozitsky O, Sagalianov I, Matzui L, Launets V (2017) Microwave properties of one-dimensional photonic structures based on composite layers filled with nanocarbon. Nanoscale Res Lett 12:269
30. Demésy G, John S (2012) Solar energy trapping with modulated silicon nanowire photonic crystals. J Appl Phys 112:074326
31. Krauss T, Rue RDL (1999) Photonic crystals in the optical regime–past, present and future. Prog Quantum Electron 23:51–96
32. Meaney P, Fox C, Geimer S, Paulsen K (2017) Electrical characterization of glycerin: water mixtures: implications for use as a coupling medium in microwave tomography. IEEE Trans Microw Theory Tech 65(5):1471–1478
33. Glycerine Producers' Association (1963) Physical properties of glycerine and its solutions. Glycerine Producers' Association, New York
34. Ruuth S (1994) Implicit-explicit methods for reaction-diffusion problems in pattern formation. J Math Biol 34:148–176
35. Volpert V (2014) Elliptic partial differential equations, volume 2: reaction–diffusion equations, monographs in mathematics, vol 104. Birkhäuser, Basel
36. Zeldovich Y, Frank-Kamenetskii D (1938) A theory of thermal propagation of flame. Acta Physicochim 9:341–350
37. Hill J, Marchant T (1996) Modelling microwave heating. Appl Math Model 20:3–15